

Published in final edited form as:

*Appl Opt.* 2014 November 10; 53(32): 7787–7795.

## rPLR: an imaging system for measuring pupillary light reflex at a distance

Dinalankara M. R. Dinalankara<sup>1</sup>, Judith H. Miles<sup>2</sup>, and Gang Yao<sup>1,\*</sup>

<sup>1</sup>Department of Bioengineering, University of Missouri, Columbia, Missouri 65211, USA

<sup>2</sup>Thompson Center for Autism and Neurodevelopmental Disorders, University of Missouri, Columbia, Missouri 65211, USA

### Abstract

Pupillary light reflex (PLR) is a simple noninvasive neurological test that can reveal a great amount of information of the neural system. We report here a novel imaging system for measuring PLR without using any restraints to limit the subject's movement. Our system incorporates a tracking component that can locate the subject's eye position and redirect the pupillary imaging component to follow the subject's movement. This system can measure PLR, at a distance from the subject, with high spatial resolution ( $<50\ \mu\text{m}$ ) and temporal resolution (120 Hz). Because this new PLR device can accommodate the subject's movement, it is well positioned to test in young children and other people who have difficulty remaining voluntarily still during tests.

### 1. Introduction

Pupil light reflex (PLR) describes the phenomena that the pupil size changes in response to illumination changes at the retina. Pupil size is controlled by two antagonistic muscles in the iris: the sphincter and dilator, which are modulated by the parasympathetic and sympathetic innervation to constrict and dilate, respectively [1]. Dysfunctions in any part along the PLR pathway including the retina, optical tract, pretectal nucleus, midbrain nucleus, and ciliary ganglion may alter the normal PLR response. Pupillary response is conventionally used as a quick test for brain injury in the emergency room by flashing a medical penlight on the eyes. With the assistance of computerized quantitative measurements, PLR has emerged as a potential noninvasive test for identifying various ophthalmological disorders and neurological disorders [2–8].

In a typical PLR measurement, images of the pupil are continuously acquired for a period from a few seconds to minutes while the subject's eye is stimulated using an optical flash with a predetermined intensity, duration, and spectrum. An image processing method is then applied to calculate the pupil size (area or radius) before, during, and after the optical stimulation. The obtained "pupilogram" curve describes the temporal course of pupil size

changes, from which multiple PLR parameters such as constriction amplitude, latency, constriction, and recovery time can be calculated.

Achieving high spatial and temporal resolutions is critical to measure small and transient pupillary responses. A variety of “pupillography” systems are available for PLR measurements. Desktop systems are the most widely used pupillography systems in PLR studies. A typical desktop PLR system usually has a spatial resolution of 15–100  $\mu\text{m}/\text{pixel}$  with an image acquisition speed of 60–120 Hz [8–14]. To achieve such a high spatial resolution, the testing subject’s head movement is usually restrained using a chin rest. A hand-held PLR device is also commercially available [15] and can achieve 50  $\mu\text{m}/\text{pixel}$  spatial resolution and 32 fps image acquisition speed. For absolute pupil size measurement, this device uses a special cone-shaped eyecup extender to maintain a constant distance between the eye and the device. This hand-held device has been extensively tested in emergence medicine [16]. In addition, custom-built head-mounted or goggle-mounted PLR devices also have been reported in literature [17–19].

Although existing pupillography devices are valuable in many applications, they are not ideal to test in young children and certain incompetent members of the population. Being able to test PLR in young children is important for certain applications such as for early screening of neurodevelopmental disorders [2,6]. Unfortunately, children at young ages often cannot cooperatively restrict their movement during the test. In addition, children with some neurodevelopmental disorders such as autism are often bothered with tactile contact [20,21] and cannot tolerate testing devices being in contact with their skin. Any forceful restraint would frustrate and stress the subjects, which is known to affect the PLR test results [22].

Because of the lack of appropriate PLR devices for testing in young children, many researchers have resorted to “remote” eye tracking systems [23–25]. Such systems are designed to determine the subject’s eye gazing direction and can allow the subjects to sit 40–150 cm from the device without any restraint. However, although eye-tracking devices can give pupil size data, they are usually not equipped with precisely synchronized and programmable optical stimulations, which are essential for PLR measurements. In addition, due to their different design focus, current remote eye tracking devices have inferior spatial resolution, as opposed to that of a specialized pupillography system. A significant amount of data averaging and low-pass filtering [23,24] is often applied to obtain a stable pupil size reading, which, unfortunately, greatly compromises the spatial and temporal resolution required to obtain accurate PLR parameters. Even with averaging, the measured pupil size may still have significant errors [24,25].

In this paper, we present for the first time to the best of our knowledge a new PLR system that can measure PLR at a distance from the subject and without the need of a physical restraint or attachments to the subject. The system incorporates a subcomponent to track the subject’s head movement. The subject’s eye position is then used to redirect the high-resolution pupil imaging system to remain focused on the subject’s eye. We show that this system can achieve accurate PLR measurements with high spatial and temporal resolution. For convenience, this system is referred to as “rPLR” (for remote PLR) hereafter.

## 2. Method

### A. System Configuration

Figure 1(a) shows a schematic of the overall configuration of the rPLR system. This system has two imaging cameras: a tracking camera and a pupil imaging camera. The testing subject's face is imaged by the tracking camera, a GigE CMOS camera (MV1-D1312, PhotonFocus AG, Lachen, Switzerland), which is equipped with an  $f = 25$  mm imaging lens. Only an  $800 \times 700$  pixel region of interest (ROI) is acquired from the camera. The tracking camera covers an imaging space of  $15.62^\circ \times 13.67^\circ$  in the horizontal and vertical directions, respectively, and with a spatial resolution of  $0.019^\circ/\text{pixel}$  or  $340 \mu\text{m}/\text{pixel}$  at a distance of 100 cm.

The high-resolution pupil images of one chosen eye are acquired using another  $640 \times 480$  CCD camera with a GigE interface (Genie HM640, Teledyne Dalsa Inc., Ontario, Canada). This pupil imaging camera uses a custom-build telescopic lens system constructed using an  $f = 75$  mm objective lens and an  $f = -25$  mm eyepiece. To implement autofocus, the divergent eyepiece is mounted on a micro-piezoelectric stage (M3-F, New Scale Technologies Inc., New York, USA). This stage has a linear translational range of 1.5 mm, which results in an overall active focusing range of 24 cm for the current optic setup. The pupil imaging system achieves a spatial resolution of  $24.0\text{--}30.2 \mu\text{m}/\text{pixel}$  over an imaging distance of 94–118 cm.

The tracking and pupil cameras are aligned coaxially using a beam splitter. The tracking camera has a lower spatial resolution and a larger field of view than the pupil imaging camera. In other words, a single pixel in the tracking camera receives more incoming light. Therefore, the beam splitter delivers 80% of the incoming light to the pupil camera and 20% to the tracking camera. The imaging direction of the entire system is steered through a 2D galvanometer scanner (6240H, Cambridge Technologies Inc., Massachusetts, USA) [26]. This scanner has a 1.5–2.0 ms response time for small angle ( $0.1^\circ$ ) rotations.

To maintain constant imaging illumination at different room light, a near-infrared (NIR) LED panel is installed outside the rPLR enclosure [Fig. 1(a)]. Such off-axis arrangement in relation to the imaging axis leads to the dark appearance of the pupil in the images, i.e., the “dark-pupil” scheme. The illumination source is constructed using an array of 96 high-power LEDs at an 850 nm central wavelength (SFH4236, OSRAM Opto Semiconductor, Michigan, USA). Accordingly, long-pass filters with a cut-off wavelength at 800 nm are installed in both cameras to block the visible ambient light. The maximal illumination intensity at the position of a subject is limited to  $75 \text{ W}/\text{m}^2$ , which is below the exposure standard ( $100 \text{ W}/\text{m}^2$  for exposure duration longer than 1000 s) recommended by the International Commission on Non-Ionizing Radiation Protection [27]. Due to the limited sensitivity of the pupil camera, an illumination intensity of  $40 \text{ W}/\text{m}^2$  is needed to achieve a clear pupil image. This effectively limits the imaging volume of the current rPLR system to a box of  $30 \text{ cm} \times 20 \text{ cm} \times 20 \text{ cm}$  ( $W \times H \times D$ ) when measured from 94 cm away from the pupil camera (calculated from the front lens of the autofocus unit).

For PLR measurements, an optical stimulation is generated by flashing a projection screen using a 530 nm green LED (LXMR-M0100-10S, Quadica Developments Inc., Ontario, Canada). Human vision has better sensitivity at green wavelengths. The LED is installed close to a projector that is ceiling-mounted in the testing room [Fig. 1(b)]. The projection screen (152 cm  $\times$  122 cm in W  $\times$  H) is installed on the wall facing the subject who sits 152–176 cm away from screen. The stimulation intensity is controlled by using neutral density optical filters and adjusting the driving current to the LED. Illuminating a large screen provides a homogeneous stimulation. The stimulation intensity was measured using a power meter (1830-C, Newport Corp., CA) and had 8% variation within the 30 cm  $\times$  20 cm  $\times$  20 cm imaging volume. During the test, videos or pictures can be displayed on the central region of the screen (56 cm  $\times$  82 cm in H  $\times$  W) to help maintain the subject's attention on the screen center.

## B. System Control

Image acquisition from the tracking and pupil cameras is synchronized and triggered using two TTL signals generated from a data acquisition (DAQ) device (PCI6259, National Instruments, Austin, TX). The image acquisition rates are 40 and 120 Hz for the tracking and pupil cameras, respectively, and the exposure time is 5.0 and 8.0 ms, respectively. The 2D galvanometer scanner is driven by control signals generated from the same DAQ board. A joystick is used as an additional interface to facilitate the manual control of the scanner. The entire system control program is developed using LabVIEW software (National Instruments, Austin, TX).

Figure 2 illustrates the overall rPLR system controls. During a typical PLR test, the tracking camera continuously acquires the subject's face images from which the subject's eye position is determined in the 3D space. If the subject's eye moves, the galvanometer scanners are rotated to redirect the imaging axis to the predicted next position of the eye. In addition, the focusing of the pupil camera is adjusted accordingly to maintain focus on the subject's eye. When the operator starts a PLR acquisition, the system begins to save pupil images to a computer, and a synchronized pulse (0.1 s) is sent 0.5 s later to turn on the stimulation LED to induce a PLR. The pupil image acquisition continues for 3.0 s in each recording episode. All aforementioned parameters can be adjusted from the system control software.

## C. Eye Detection

Eye detection is the key function of the rPLR system. From the tracking camera, the glint (the first Purkinjer image) [28] of the NIR LED array is used to identify the eye location. Because the glint is usually the brightest spot in the image, a  $3 \times 3$  Sobel filter is first applied to the tracking image to locate the glint. The glint intensity may not be identical in the left and right eyes due to different illumination angles and intensities at the two eyes. Therefore, a different threshold is determined for each glint by identifying the two pixels with the highest edge values. After the pixel with the highest edge value is identified, its surrounding area of  $100 \times 100$  pixels is excluded from searching for the pixel with the second-highest edge value to prevent erroneous results from tears and eye boundaries.

A regular person blinks at the rate of  $16 \pm 8.4 \text{ min}^{-1}$  [29]. When an eye blinks, the pupil is covered and cannot be detected correctly. Therefore, blinking events need to be identified and excluded from the analysis to ensure accurate eye detection. Because the glint appears on the eyelid during blinking, it has a smaller edge value than the true glint located inside a dark pupil or iris region [Fig. 3(a)]. In other words, the blinking can be identified based on its lower edge value. However, the specific edge value is affected by the subject's skin color. In order to determine the blinking threshold for each individual subject, the highest edge values in tracking images are recorded and analyzed for a few sessions with a 10 s recording in each session. From the histogram of those recorded glint edge values [Fig. 3(b)], the midpoint between the two peaks is chosen as the blink threshold [shown as the dashed line in Fig. 3(b)].

Once the glint is detected for open eyes, the image pixels surrounding the glint are further analyzed to find the center of the pupil. First, the histogram of a region of interest around the glint is constructed. Due to the dark pupil, the first minima of the histogram is applied as the threshold value to extract the pupil. Then an edge detector is applied on the extracted pupil image to obtain the pupil border. The center of the pupil is located by applying an ellipse fitting on all pixels on the pupil boundary. If both eyes are present, the center pixel of the left and right pupils is obtained separately and identified according to their relative positions in the image.

To ensure the accuracy of eye detection, the calculated glint and pupil center in the current tracking image are compared with those obtained in the previous frame. The current glint/pupil center is validated if its distance from the previous frame is smaller than the inter-pupillary distance (IPD), which is defined as the distance between the two pupil centers. If a blink is detected, the tracking for the current frame is invalidated, and the system waits for the next image. If only one eye is detected, the position of this eye is compared with that of the previously detected eyes to determine whether it is the right or left eye. Then the corresponding eye position is validated and updated. The current position of the other eye is calculated based on its relative position recorded in the previous frame. If no eye is validated, the last validated eye centers are used.

#### D. Eye Position Prediction and Autofocusing

The rPLR system automatically steers its imaging axis so that the detected pupil remains at the center of the pupil camera images. A simple linear prediction algorithm is implemented to predict the next position of the pupil center. The pixel position of the pupil center in the image plane can be converted into angular positions  $\theta_{\text{IMG}}$  because the tracking camera uses a lens with a fixed focal length. The angular position in the object space can be obtained as  $\theta = M \times \theta_{\text{IMG}}$ , where  $M$  is a precalibrated coefficient for the tracking imaging system. The next angular position  $\theta_{x,y}(t+1)$  can be predicted using linear angular motion equations based on estimated angular velocity and acceleration from the previous two positions:

$$\begin{aligned}\theta_{x,y}(t+1) &= \theta_{x,y}(t) + \dot{\theta}_{x,y}(t)\Delta t + \ddot{\theta}_{x,y}(t)\Delta t^2/2 \\ \dot{\theta}_{x,y}(t) &= [\theta_{x,y}(t) - \theta_{x,y}(t-1)]/\Delta t \\ \ddot{\theta}_{x,y}(t) &= [\theta_{x,y}(t) - 2\theta_{x,y}(t-1) + \theta_{x,y}(t-2)]/\Delta t^2,\end{aligned}\quad (1)$$

where  $\theta_{x,y}(t)$  represents the current angle of the pupil center along the horizontal ( $x$ ) and vertical ( $y$ ) directions;  $t$  is the time interval between two frames. The 2D galvanometer scanner is then turned by applying appropriate driving voltages to match this predicted new angular position.

The distance ( $D$ ) between the eye and the imaging system is estimated based on the subject's IPD, which is measured prior to the test using a ruler. The corresponding pupil center distance in the image field  $IPD_{IMG}$  can be approximately related to the actual IPD based on the following geometric relationship:

$$\tan^{-1}\left(\frac{IPD}{D}\right) = M \tan^{-1}\left(\frac{IPD_{IMG}}{f}\right), \quad (2)$$

where  $f$  is the focal length of the tracking camera lens;  $IPD_{IMG}$  is the measured distance between the two pupil centers in the tracking image; and  $M$  is a precalibrated coefficient for the tracking imaging system. The distance  $D$  can then be derived as

$$D = \frac{IPD}{\tan[M \tan^{-1}(IPD_{IMG}/f)]}. \quad (3)$$

Once this distance  $D$  is calculated, the imaging lens of the pupil camera is adjusted to focus on the pupil using a precalibrated curve on the position of the eyepiece.

### 3. Results

#### A. Motion Tracking

The rPLR system's tracking capability was first tested using a spherical testing target mounted on a motorized linear stage (ILS50CC, Newport Corp., CA). The testing target was positioned at 100 cm away from the rPLR device. The center of the sphere was used to simulate the pupil center. Instead of the pupil identification method described in Section 2.C, a simple algorithm based on the LabVIEW pattern recognition toolbox was used to identify the sphere target. The speed of the stage was set randomly between 3 ~ 10 cm/s, and its acceleration was set to 40 cm/s<sup>2</sup>. The moving position of the target was randomly selected to monitor the prediction performance under random motion. The difference between the observed and predicted sphere center was calculated to assess the tracking performance.

As the tracking camera detects the angular position of the target [Eq. (1)], the prediction error can be calculated as the difference between the actual angular position and the predicted angular position. For convenience, the angular values can be converted into imaging pixels based on the angular resolution of the tracking system described in Section 2.A. Based on the imaging fields of the tracking and pupil cameras, the pupil can stay in the middle of the pupil image if the prediction error remains less than 8 pixels or ~0.15° in the tracking image system. Figure 4(a) shows a typical result obtained in a 120 s recording, where more than 99.4% measurements had a prediction error of less than 8 pixels. The error distribution can be fitted using a Gaussian function ( $R^2 = 0.99$ ), as shown by a dashed line in

Fig. 4(a). The fitted mean prediction error is 0.9 pixels, and the standard deviation is 1.8 pixels.

Although a typical human head moving speed is usually less than 10 cm/s during the test, human subject movement may be more unpredictable. Therefore, we tested the tracking performance in human subjects moving at different speeds. The actual eye position and prediction were measured and recorded as described in the Method section. The speed was calculated as the first derivative of the position data. Figure 4(b) shows a test where a subject intentionally moved left–right at speeds up to 15 cm/s. More than 50% of the movement was accurately predicted, and 99.2% of the prediction came within the 8 pixel margin. The prediction error increased at a higher movement speed. Figure 4(d) shows an example where the subject intentionally moved faster with a speed up to 25 cm/s. In this case, only ~30% of the prediction had a zero pixel error, but 92.4% of the overall prediction was still within 8 pixels.

## B. Pupil Image Resolution and Auto Focusing

The resolution of the pupil imaging system was verified by imaging a USAF 1951 resolution chart placed at 94 cm from the pupil camera. The third group sixth element of the resolution chart can be clearly seen, and the fourth group first element is vaguely visible. These results indicated an imaging resolution of better than 14.40 line pairs/mm or 34.97  $\mu\text{m}$  of a single line.

The autofocus system is designed to maintain an effective focusing on eyes positioned at 94–118 cm from the pupil camera. To evaluate the focusing effect, we first examined the focusing effect by imaging a USAF 1951 resolution chart placed at 96, 104, and 114 cm from the pupil camera. For each target position, a series of images were acquired when the focus was adjusted from 94–118 cm with a 1.0 cm step size. To estimate image sharpness, a  $3 \times 3$  Sobel filter was first applied to the images. The total number of pixels whose pixel value was greater than 0.02 in the edge-filtered images was used as the sharpness value. The sharpness values were normalized by the value obtained at the correct focusing distance in the corresponding image sequence.

As shown in Fig. 5, in all three cases, the image sharpness maintained the same maximum value over a distance of ~2 cm when the focusing distance was coincident with its position. Within this 2 cm distance, the images appeared sharp without any discernible differences. This value is similar to the theoretical depth of focus (DoF) of 2.5 ~ 3.5 cm calculated using the following equation [30]:

$$\text{DoF} = \frac{2Ncf^2u^2}{f^4 - N^2c^2u^2}, \quad (4)$$

where  $c$  is the circle of confusion (twice the pixel size, 14.8  $\mu\text{m}$ ),  $f$  is the effective focal length (from 13.8 to 15.5 cm),  $N$  is the  $f$ -number (18.4–20.7), and  $u$  is the object distance (from 94 to 118 cm).



Figures 6(a) and 6(b) demonstrate the effect of autofocus in a human subject who intentionally moved back and forth during the test. The speed of the movement was estimated as 8–13 cm/s. The sharpness curves were normalized with the values obtained within the first 0.5 s of the measurements when the subject was relatively still. Sharp pupil images were obtained before the subject started to move. Without enabling autofocus, the image sharpness decreased dramatically once the movement started. As shown in the enclosed images in Fig. 6(a), pupil images were significantly blurred at 3 and 7 s when the subject was 10–12 cm away from the original position. The image sharpness was recovered when the subject moved back to the initial position. When autofocus was enabled, clear pupil images were obtained throughout the test, as shown in Fig. 6(b). The sharpness curve still had some fluctuations, although the pupil images showed little difference in sharpness. Such fluctuation may be partially attributed to the subtle motion-induced blurring, which was limited by the exposure time. It also can be caused by pupil size changes during movement, which changed the number of pixels at the pupil boundary after edge detection. Nevertheless, the results shown in Fig. 6 verify the effectiveness of autofocusing.

### C. PLR Test

During a typical PLR test, a subject is seated in front of the rPLR system and watches a movie projected on the screen, as shown in Fig. 1(b). The rPLR system automatically detects the pupil, aligns the imaging axis, and sets the focusing. If the initial positions of the subject's eyes are outside the imaging region, the test operator can manually set the scanner positions using the joystick, as described in Section 2.B. The blink threshold is automatically analyzed, as described in Section 2.C. The operator can start a PLR test episode at will thereafter. Because the captured pupil size changes with the subject's distance, the measured pupil size is corrected based on the subject's position using a calibration curve.

We conducted some pilot testing in human subjects. The tests are conducted at two room-illuminance conditions: 5.6 and 2.7 lx. The 5.6 lx illuminance was obtained with the room light on, whereas the 2.7 lx illuminance was obtained when the room light was turned off. Without the room light, the remaining room illuminance was from the NIR light source and the movie/image (red-filtered) shown on the projector screen. PLRs were measured first at 5.6 lx room illuminance and then measured again 10 min after turning the room light off. The pupil camera was set to image the subject's right eye in the tests. Multiple tests were acquired at each condition. We waited at least 20 s between the two consecutive PLR tests, so that the pupil could fully recover from the previous stimulation. The recorded pupil images were processed using the image process procedure described previously [11] to extract the pupil size data to construct the pupilogram.

Figure 7 shows two example pupilograms. The 0.1 s optical stimulation was given at 0.5 s. As expected, the baseline pupil size ("resting pupil size") was larger at weaker room illuminance. Both curves in Fig. 7(a) show the standard pupillary response to a brief optical stimulation, i.e., a rapid constriction after a delay and then a slower recovery to the baseline. From the pupilogram, multiple PLR parameters can be extracted such as the constriction



amplitude, latency, constriction time, and constriction speed using image processing, as described in [11,31].

As examples, Figs. 7(b) and 7(c) show the extracted relative constriction and latency at stimulation intensities from  $4.5 \times 10^{-5}$  to  $2.8 \times 10^{-3}$  W/m<sup>2</sup>. PLR constriction and latency are often used in study neurological disorders [6,11]. The relative constriction is defined as the change of pupil size in relation to the baseline pupil size. The PLR latency is defined as the delay between the optical stimulation and when pupil starts to constrict. As shown in Figs. 7(b) and 7(c), the PLR latency decreases and the constriction increases with the stimulation intensity. At the same stimulation intensity, the PLR constriction was much higher at darker room illuminance while PLR latency was smaller. The PLR constriction increased linearly with the log of stimulation intensity. Consistent PLR constriction from <10% to over 50% was reliably measured. The measured latency ranged from 0.20 to 0.28 s under the stimulation conditions. These values are in good agreement with previous reports obtained using a traditional desktop pupillography system [31].

#### 4. Discussion

Tracking the subject's eye is the key feature of the rPLR system. By steering the pupil imaging system to follow the subject's eye, this system can reliably measure PLR without the need to use physical restraint to fix the subject's eye position. The tracking system detects the subject's eye based on the glint detection. Therefore, the presence of a high-reflecting substance such as an earring or oil may lead to incorrect glint detection, as they make high edge values as true glint. Although eye blinks can be reliably detected using our method, invalid glint detection can still happen if the subject's eyes remain partially open and the eyelids cover the majority of the iris. The current tracking volume is limited mainly by the NIR source's coverage. A larger imaging volume is possible if the NIR source is designed to cover a larger area or a steering mechanism is used to redirect the NIR illumination to follow the subject's movement.

The current system configuration works reliably if the subject moves at a speed less than 25 cm/s. Although this is sufficient for most natural human movement in a testing environment, it is possible that a subject may move faster. The overall tracking speed is determined by the image acquisition speed, image processing time, and the scanner's response. The speed of the tracking camera can be easily increased, and the response time of the galvanometers can be enhanced by using mirrors of lighter weight. The image processing time is currently the primary limitation for faster tracking. It can be further improved by using more efficient implementation.

The current autofocus implementation uses a simple algorithm based on the premeasured IPD. The major consideration of such an implementation is the computation speed. One limitation of this method is that the calculation becomes less accurate when the subject's face is not parallel to the imaging plane. However, the ~2 cm depth-of-focus of the pupil imaging system can well tolerate a ~25° range of rotation or tilting of the head without suffering noticeable deterioration in imaging sharpness. In addition, our system control is equipped with an external joystick, so that the operator can manually adjust the focus when

necessary. Autofocusing also can be implemented using an adaptive lens [32,33]. More sophisticated autofocus algorithms may be implemented at the expense of a more complicated system and higher computational demand [34–36].

## 5. Conclusion

In this paper, we described and demonstrated a novel pupillography system that allows the subject to sit freely during the PLR test instead of keeping the head in a still position. Pupillary imaging at high spatial resolution (30  $\mu\text{m}/\text{pixel}$  or  $0.0015^\circ/\text{pixel}$ ) was achieved at a frame rate of 120 Hz. The current system allows imaging of one selected pupil and can be expanded by adding a second pupil camera for binocular PLR tests. Because this new PLR device can accommodate the subject's movement, it is well positioned to test in young children and other members of the population who have difficulty remaining voluntarily still during tests.

## Acknowledgments

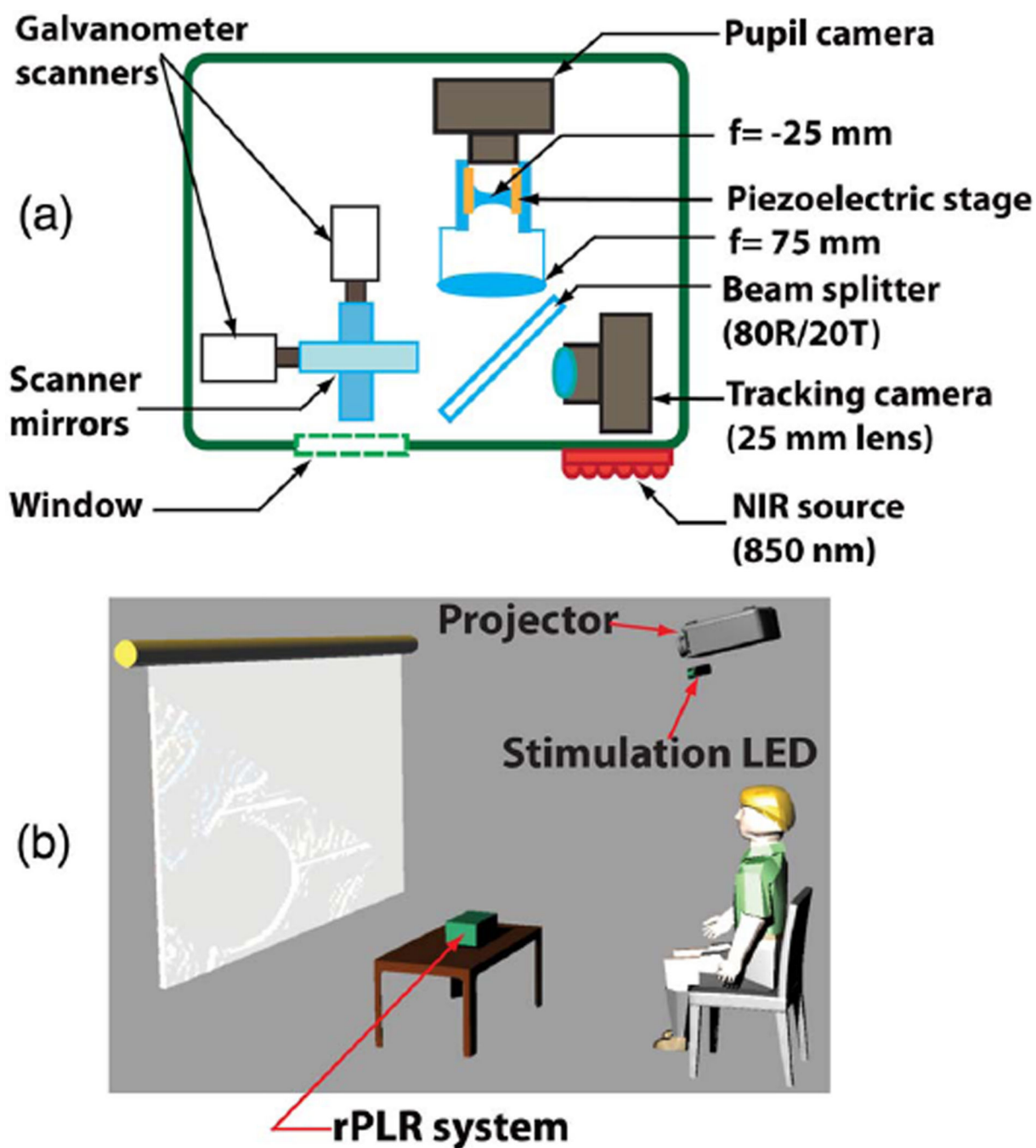
This work was supported in part by the Eunice Kennedy Shriver National Institute of Child Health and Human Development (NICHD) under grant R21-HD075971, and the Coulter Translational Partnership at University of Missouri.

## References

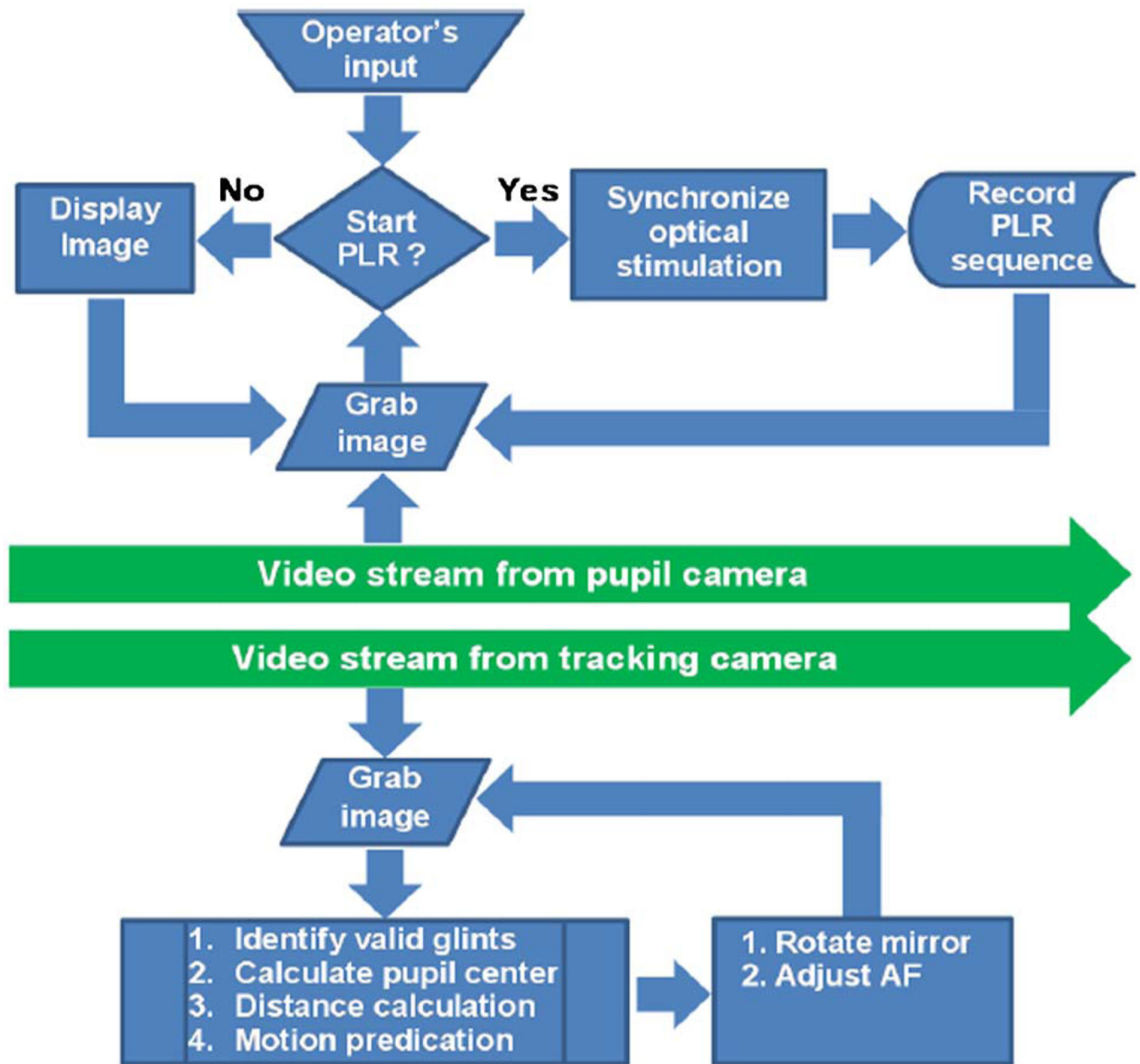
1. Barbur, JL. The Visual Neurosciences. Vol. 1 and 2. MIT; 2004. Learning from the pupil studies of basic mechanisms and clinical applications; p. 641-656.
2. Fan X, Miles JH, Takahashi N, Yao G. Abnormal transient pupillary light reflex in individuals with autism spectrum disorders. *J. Autism Dev. Disord.* 2009; 39:1499–1508. [PubMed: 19499319]
3. Ferrari GL, Marques JLB, Gandhi RA, Heller SR, Schneider FK, Tesfaye S, Gamba HR. Using dynamic pupillometry as a simple screening tool to detect autonomic neuropathy in patients with diabetes: a pilot study. <http://www.biomedical-engineering-online.com/content/9/1/26>.
4. Giza E, Fotiou D, Bostantjopoulou S, Katsarou Z, Karlovasitou A. Pupil light reflex in Parkinson's disease: evaluation with pupillometry. *Int. J. Neurosci.* 2011; 121:37–43. [PubMed: 21034369]
5. Farzin F, Scaggs F, Hervey C, Berry-Kravis E, Hessler D. Reliability of eye tracking and pupillometry measures in individuals with fragile X syndrome. *J. Autism Dev. Disord.* 2011; 41:1515–1522. [PubMed: 21267642]
6. Daluwatte C, Miles JH, Christ SE, Beversdorf DQ, Takahashi TN, Yao G. Atypical pupillary light reflex and heart rate variability in children with autism spectrum disorder. *J. Autism Dev. Disord.* 2013; 43:1910–1925. [PubMed: 23248075]
7. Muppidi S, Adams-Huet B, Tajzoy E, Scribner M, Blazek P, Spaeth EB, Frohman E, Davis S, Vernino S. Dynamic pupillometry as an autonomic testing tool. *Clin. Auton. Res.* 2013; 23:297–303. [PubMed: 23880969]
8. Bergamin O, Kardon RH. Latency of the pupil light reflex: sample rate, stimulus intensity, and variation in normal subjects. *Investig. Ophthalmol. Vis. Sci.* 2003; 44:1546–1554. [PubMed: 12657591]
9. Granholm E, Morris S, Galasko D, Shults C, Rogers E, Vukob B. Tropicamide effects on pupil size and pupillary light reflexes in Alzheimer's and Parkinson's disease. *Int. J. Psychophysiol.* 2003; 47:95–115. [PubMed: 12568941]
10. Fotiou DF, Brozou CG, Tsitsios DJ, Fotiou A, Kabitsi A, Nakou N, Giantselidis C, Goula A. Effect of age on pupillary light reflex: evaluation of pupil mobility for clinical practice and research. *Electromyogr. Clin. Neurophysiol.* 2007; 47:11–22. [PubMed: 17375877]

11. Fan X, Miles JH, Takahashi N, Yao G. Sex-specific lateralization of contraction anisocoria in transient pupillary light reflex. *Investig. Ophthalmol. Vis. Sci.* 2009; 50:1137–1144. [PubMed: 18836163]
12. Gabay S, Pertzov Y, Henik A. Orienting of attention, pupil size, and the norepinephrine system. *Atten. Percept. Psychophys.* 2011; 73:123–129.
13. Gagl B, Hawelka S, Hutzler F. Systematic influence of gaze position on pupil size measurement: analysis and correction. *Behav. Res. Methods.* 2011; 43:1171–1181. [PubMed: 21637943]
14. Sabeti F, James AC, Essex RW, Maddess T. Multifocal pupillometry identifies retinal dysfunction in early age-related macular degeneration. *Graefes Arch. Clin. Exp. Ophthalmol.* 2013; 251:1707–1716. [PubMed: 23392820]
15. Meeker M, Du R, Bacchetti P, Privitera CM, Larson MD, Holland MC, Manley G. Pupil examination: validity and clinical utility of an automated pupillometer. *J. Neurosci. Nurs.* 2005; 37:34–40. [PubMed: 15794443]
16. Taylor WR, Chen JW, Meltzer H, Gennarelli TA, Kelbch C, Knowlton S, Richardson J, Lutch MJ, Farin A, Hults KN, Marshall LF. Quantitative pupillometry, a new technology: normative data and preliminary observations in patients with acute head injury—technical note. *J. Neurosurg.* 2003; 98:205–213. [PubMed: 12546375]
17. Tales A, Troschianko T, Lush D, Haworth J, Wilcock GK, Butler SR. The pupillary light reflex in aging and Alzheimer's disease. *Aging-Clin. Exp. Res.* 2001; 13:473–478.
18. Kardon R, Anderson SC, Damarjian TG, Grace EM, Stone E, Kawasaki A. Chromatic pupil responses: preferential activation of the melanopsin-mediated versus outer photoreceptor-mediated pupil light reflex. *Ophthalmology.* 2009; 116:1564–1573. [PubMed: 19501408]
19. de Souza JKS, da Silva Pinto MA, Vieira PG, Baron J, Tierra-Criollo CJ. An open-source, firewire camera-based, labview-controlled image acquisition system for automated, dynamic pupillometry and blink detection. *Comput. Methods Prog. Biomed.* 2013; 112:607–623.
20. Ashburner J, Ziviani J, Rodger S. Sensory processing and classroom emotional, behavioral, and educational outcomes in children with autism spectrum disorder. *Am. J. Occup. Ther.* 2008; 62:564–573. [PubMed: 18826017]
21. Tomchek SD, Dunn W. Sensory processing in children with and without autism: a comparative study using the short sensory profile. *Am. J. Occup. Ther.* 2007; 61:190–200. [PubMed: 17436841]
22. Davis BC, Daluwatte C, Colona NC, Yao G. Effects of cold-pressor and mental arithmetic on pupillary light reflex. *Physiol. Meas.* 2013; 34:873–882. [PubMed: 23859888]
23. Klingner, J.; Kumar, R.; Hanrahan, P. Proceeding of Eye Tracking Research and Application. ACM; 2008. Measuring the task-evoked pupillary response with a remote eye tracker; p. 69-72.
24. Brisson J, Mainville M, Mailloux D, Beaulieu C, Serres J, Sirois S. Pupil diameter measurement errors as a function of gaze direction in corneal reflection eye trackers. *Behav. Res. Methods.* 2013; 45:1322–1331. [PubMed: 23468182]
25. Klingner, J. Proceeding of Eye Tracking Research and Application. ACM; 2010. The pupillometric precision of a remote video eye tracker; p. 259-262.
26. Beymer, D.; Flickner, M. Proceeding of IEEE Conference on Computer Vision and Pattern Recognition. IEEE; 2003. Eye gaze tracking using an active stereo head; p. 451-458.
27. ICNIRP. ICNIRP statement on far infrared radiation exposure. *Health Physics.* 2006; 91:630–645. [PubMed: 17099407]
28. Lee JW, Cho CW, Shin KY, Lee EC, Park KR. 3D gaze tracking method using Purkinje images on eye optical model and pupil. *Opt. Lasers Eng.* 2012; 50:736–751.
29. Skotte JH, Nojgaard JK, Jorgensen LV, Christensen KB, Sjogaard G. Eye blink frequency during different computer tasks quantified by electrooculography. *Eur. J. Appl. Physiol.* 2007; 99:113–119. [PubMed: 17115181]
30. Jacobson, RE.; Ray, SF.; Attidge, GG.; Axford, NR. *The Manual of Photography; Photographic and Digital Imaging.* Focal; 2000. The geometry of image formation; p. 39-60.
31. Fan X, Hearne L, Lei B, Miles JH, Takahashi N, Yao G. Weak gender effects on transient pupillary light reflex. *Auton. Neurosci.* 2009; 147:9–13. [PubMed: 19168398]

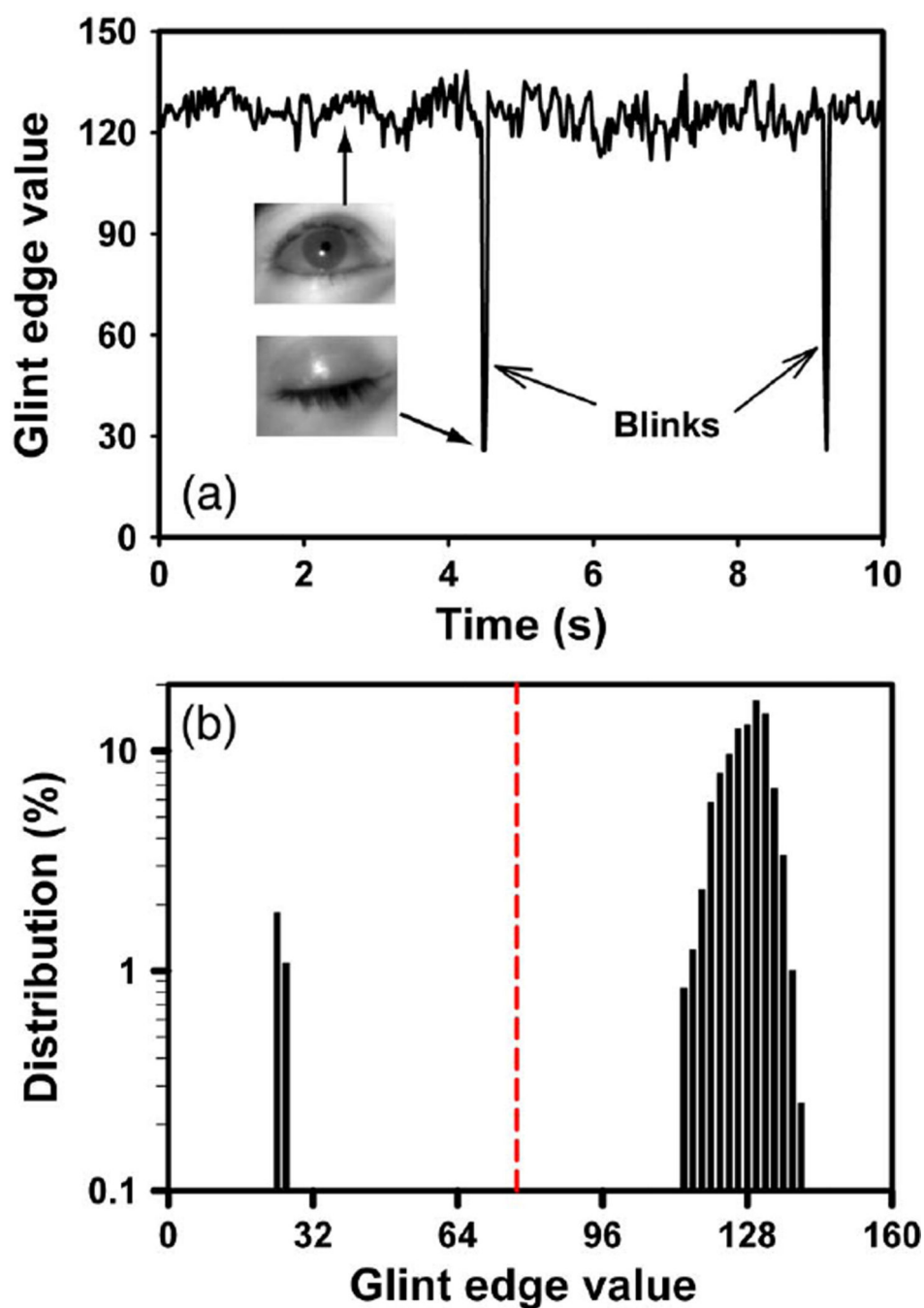
32. Li G, Mathine DL, Valley P, Äyräs P, Haddock JN, Giridhar MS, Williby G, Schwiegerling J, Meredith GR, Kippelen B, Honkanen S, Peyghambarian N. Switchable electro-optic diffractive lens with high efficiency for ophthalmic applications. *Proc. Natl. Acad. Sci.* 2006; 103:6100–6104. [PubMed: 16597675]
33. Li G. Adaptive lens. *Prog. Opt.* 2010; 55:199–283.
34. Ding X, Xu L, Wang H, Wang X, Lv G. Stereo depth estimation under different camera calibration and alignment errors. *Appl. Opt.* 2011; 50:1289–1301. [PubMed: 21460891]
35. Kuo CFJ, Chiu CH. Improved auto-focus search algorithms for CMOS image-sensing module. *J. Inf. Sci. Eng.* 2011; 27:1377–1393.
36. Khoshelham K, Elberink SO. Accuracy and resolution of kinect depth data for indoor mapping applications. *Sensors.* 2012; 12:1437–1454. [PubMed: 22438718]

**Fig. 1.**

(a) Diagram of rPLR system. (b) Illustration of the setup for a PLR test. The optical stimulation is implemented by illuminating a projection screen using an LED.

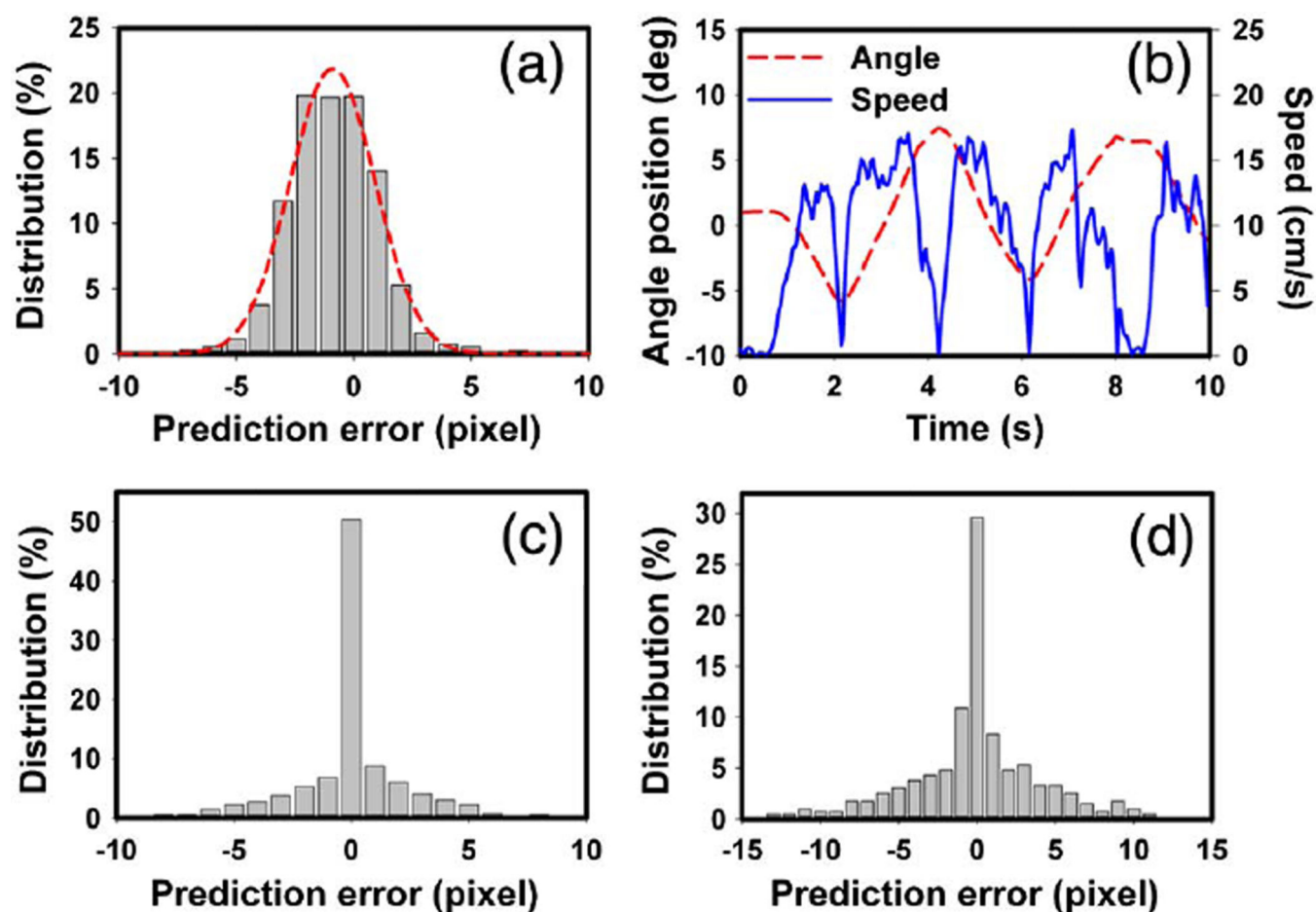


**Fig. 2.** Illustration of overall rPLR system control. The image processing procedures are independent and parallel for the tracking system and pupil imaging system.

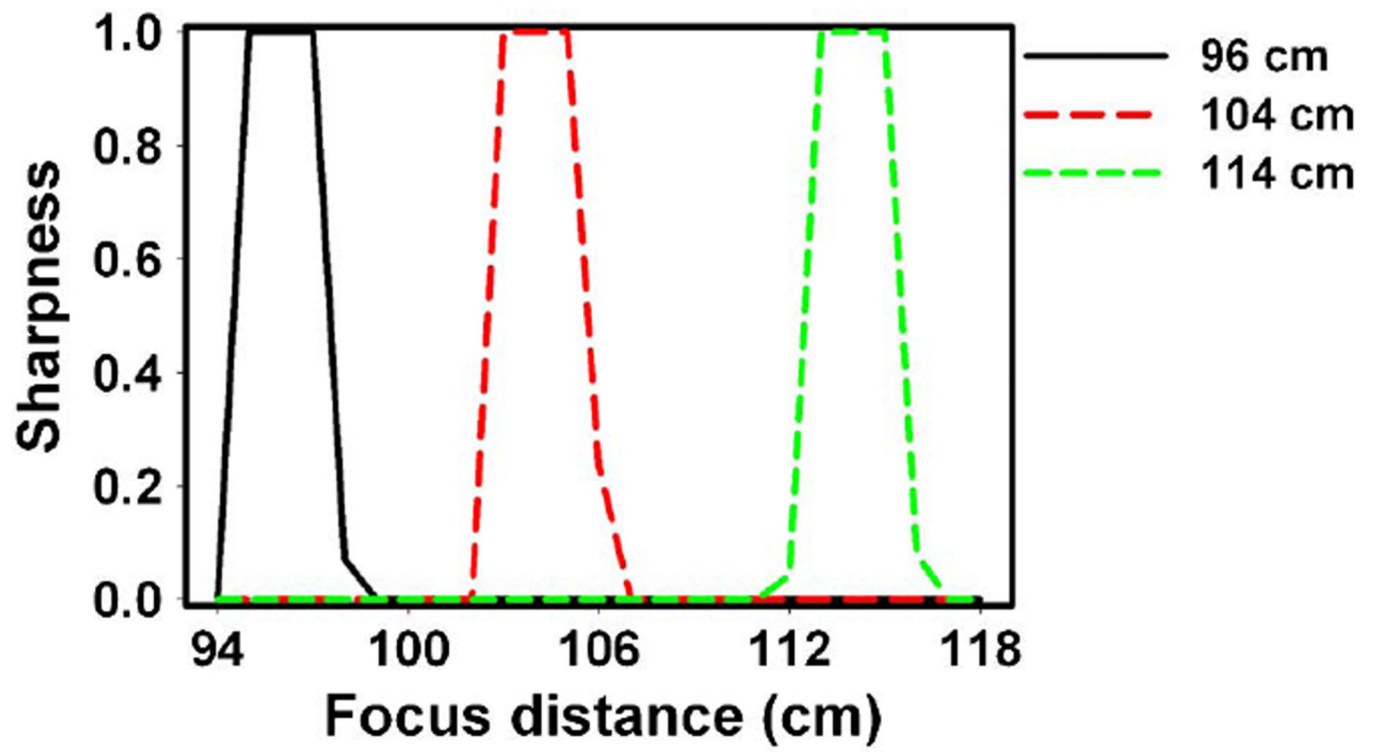


**Fig. 3.**  
 (a) The glint edge values recorded for 10 s. (b) The histogram of the measured glint edge values obtained in three 10 s recordings. The dashed line in (b) indicates the threshold chosen for identifying blinks.

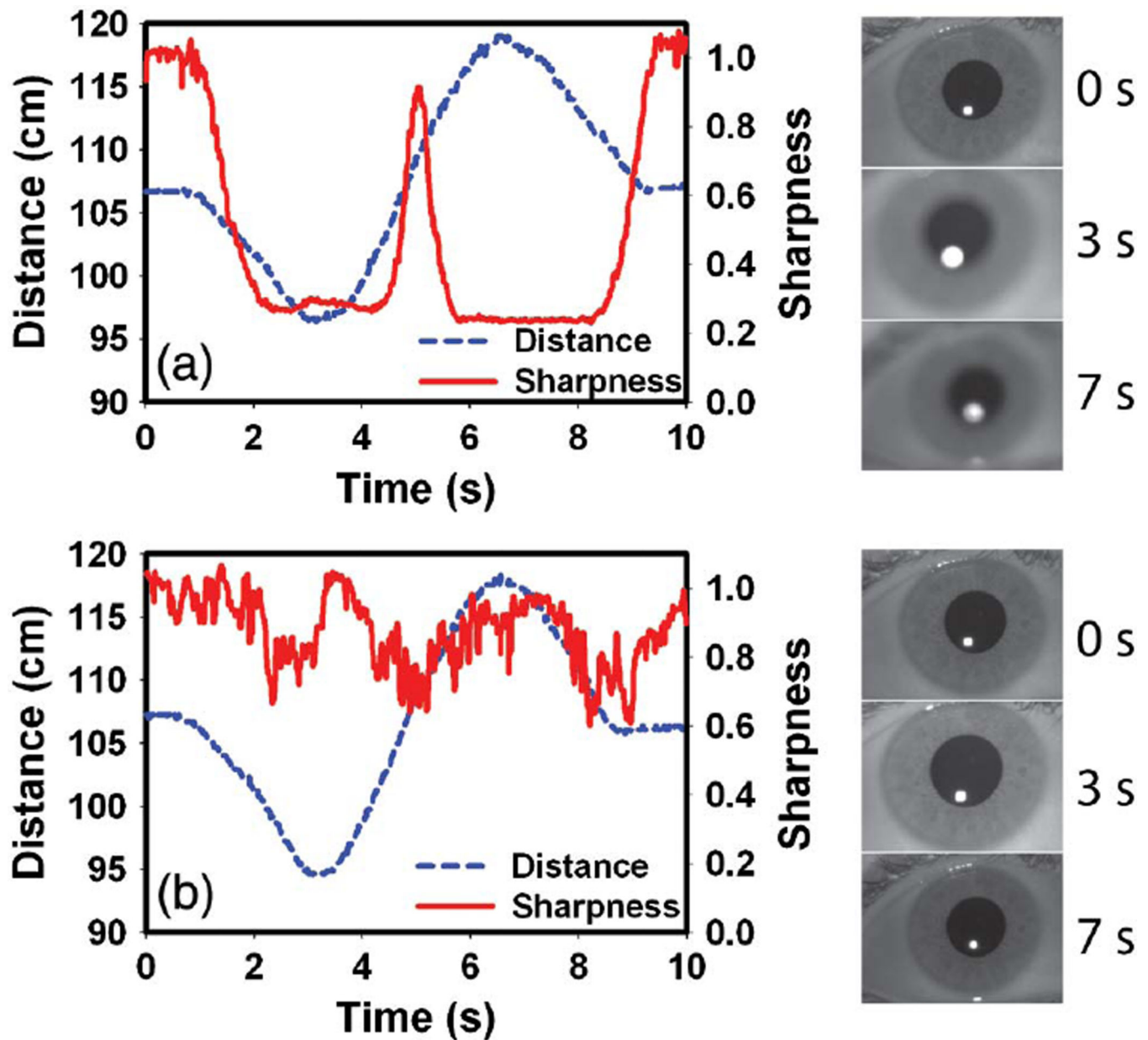




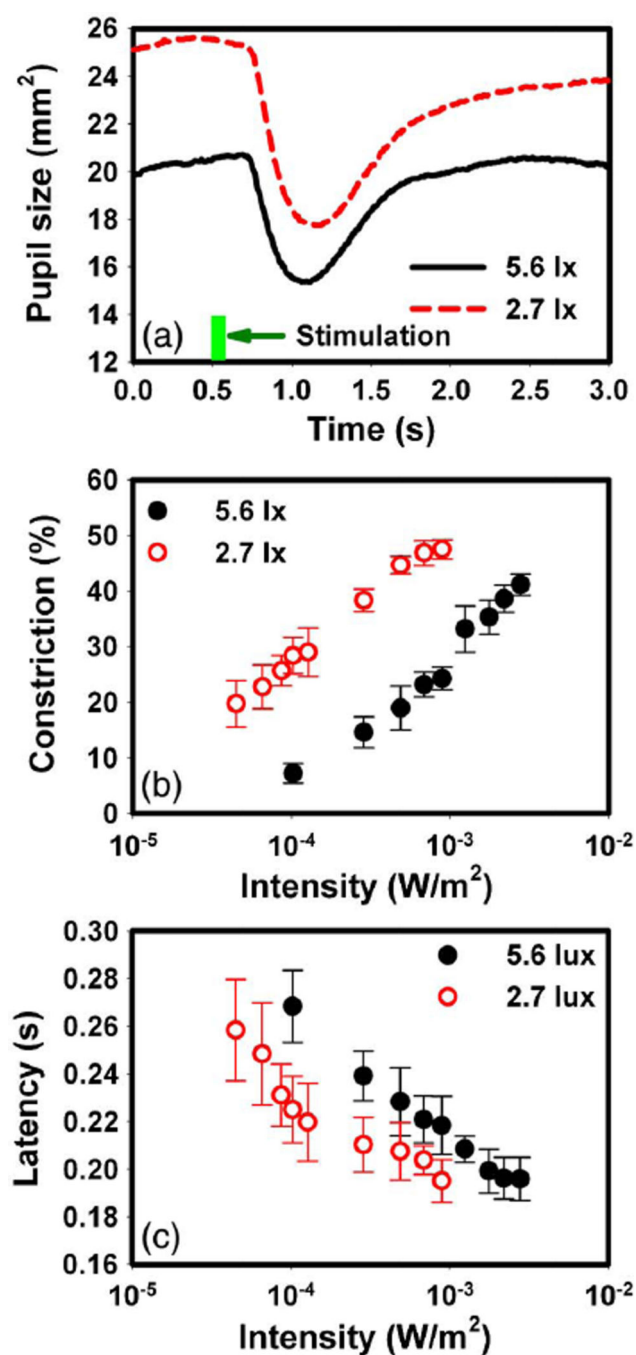
**Fig. 4.** Performance of the tracking system. (a) Distribution of tracking error for a randomly moving spherical target. (b) Movement (angular position and speed) of a human subject and (c) the corresponding tracking error. (d) Tracking error for a subject moving at a higher speed up to 25 cm/s.



**Fig. 5.** Effect of focusing on image sharpness of a USAF 1951 resolution chart placed at 96, 104, and 114 cm from the pupil camera.



**Fig. 6.** Sharpness of the pupil images of a subject moving back and forth in the test when the autofocus was (a) disabled and (b) enabled. Also shown are example pupil images acquired at three points of time. The corresponding distances at different time are plotted as dashed lines.

**Fig. 7.**

(a) Example pupilograms measured in light adaptation and dark adaptation. (b) PLR constriction and (c) latency measured at various stimulation intensities from  $4.5 \times 10^{-5}$  to  $2.8 \times 10^{-3}$  W/m<sup>2</sup>.